

Interpreting spatially stacked Sp receiver functions

Vedran Lekić¹ and Karen M. Fischer²

¹*Department of Geology, University of Maryland, College Park, MD 20742, USA. E-mail: ved@umd.edu*

²*Department of Earth, Environmental and Planetary Sciences, Brown University, Providence, RI 02912, USA*

Accepted 2017 May 11. Received 2017 May 4; in original form 2016 June 21

SUMMARY

Conversions of shear waves (S) to compressional waves (P), often analysed as Sp receiver functions, are useful for studying upper-mantle layering, and have been used to map upper-mantle seismic impedance interfaces in various tectonic settings. Recently, common conversion point (CCP) stacking of Sp receiver functions has revealed variations of lithospheric thickness across short horizontal distances. However, compared to Ps receiver functions and reflection, only limited work has been done towards quantifying the interpretability of Sp receiver functions, especially in settings where large lateral structure variations are present. Using the spectral element method, we model wave propagation and S -to- P conversion through simple synthetic models with varying velocity interface topography. We systematically explore the effects of wave frequency content, seismometer spacing and illumination geometry on CCP stacked Sp receiver functions in settings where velocity interface depth varies laterally. We observe that the resolving power of Sp receiver functions decreases with decreasing frequency content, and that upward deflections of velocity interfaces are more difficult to observe than are downward deflections, an asymmetry that primarily arises due to corner diffractions. Furthermore, we document how the relationship between the angle of illumination and the orientation of the topography of the velocity interfaces largely determines the apparent interface slope and strongly affects the amplitude of Sp phases in the CCP stacks. Indeed, under certain illumination geometries, strong velocity contrasts across a dipping lithosphere–asthenosphere boundary may not produce detectable Sp phases at the surface. Furthermore, diffractions arising from corners of interface topography can produce artefacts in CCP stacks that masquerade as mid-lithospheric impedance jumps or drops, as well as gently sloped sublithospheric impedance drops. We find that estimates based on Fresnel zone arguments might, in some cases, underestimate the true resolution, and that they are likely to be only appropriate for situations in which abrupt lateral variations in structure do not produce waveform complexities. These results imply that the interpretation of Sp receiver functions and CCP stacks is not straightforward and that care must be exercised when inferring the presence or absence of lithospheric velocity interfaces.

Key words: Time-series analysis; Body waves; Wave propagation; Wave scattering and diffraction.

1 INTRODUCTION

As they propagate upward across sufficiently sharp velocity interfaces, teleseismic waves can convert from shear (S) to compressional (P) type and vice versa, giving rise to pre- and post-cursory signals that can be observed and modelled (for recent reviews, see Rondenay 2009; Kind *et al.* 2012). While early studies of this phenomenon focused on identifying P -to- S (Ps) conversions (e.g. Burdick & Langston 1977; Vinnik 1977), the receiver-function (RF) approach has enabled routine analysis of these phases to study crustal and upper-mantle structure. However, since P -to- S conversions arrive after the main P phase, signal from sub-Moho velocity discontinuities can be obscured by multiply reflected energy arising from the Moho and impedance discontinuities in the crust (e.g. base of sediment); with S -to- P conversions, signal from deeper disconti-

nities always comes out ahead of signals arising from shallower structures (Farra & Vinnik 2000). This makes S -to- P an attractive method for probing intra- and sublithospheric structure.

Recently, modelling conversion of shear to compressional energy using the RF approach has been used to characterize sub-Moho discontinuities such as the lithosphere–asthenosphere boundary (LAB) and the continental mid-lithospheric discontinuity on regional (Angus *et al.* 2006; Chen *et al.* 2006; Li *et al.* 2007; Wittlinger & Farra 2007; Levander & Miller 2012; Wolbern *et al.* 2012; Hopper *et al.* 2014; Lekić & Fischer 2014; Hopper & Fischer 2015; Reeves *et al.* 2015; Vinnik *et al.* 2016), continental (Abt *et al.* 2010; Ford *et al.* 2010; Hansen *et al.* 2015) and global scales (Rychert & Shearer 2009; Rychert *et al.* 2010). In densely instrumented areas, common conversion point (CCP) stacking of S -to- P RFs has resolved topography on the LAB within and along

margins of cratonic settings (Chen *et al.* 2009; Miller & Eaton 2010) and steep LAB topography beneath Southern California (Lekić *et al.* 2011). The presence of laterally abrupt variations in lithospheric thickness violates the basic assumption underlying RF methods, namely, that the structure beneath the seismic receiver can be accurately represented as a stack of horizontal layers with different densities and elastic properties.

The presence of lateral variation in lithospheric structure may motivate the use of formal wavefield migration techniques (e.g. Revenaugh 1995; Sheehan *et al.* 2000; Bostock *et al.* 2001; Poppe-liers & Pavlis 2003; Levander *et al.* 2005; Wilson & Aster 2005), which can accurately model first order wavefield interaction with laterally varying structures. However, in many locations wavefield migration is not viable due to inadequate station spacing and illumination geometry. For example, Rondenay *et al.* (2005) show that operator aliasing can substantially distort images at depths less than twice the station spacing; for the EarthScope Transportable Array, this means that full wavefield migration techniques are unavailable for the study of lithospheric layering. Furthermore, the range of epicentral distances—and, therefore, coverage of ray parameter—that can be used in *S*-to-*P* studies is limited by post-critical conversion on one end, and contamination by multiply bouncing *P*-waves on the other (Wilson *et al.* 2006). This limited coverage substantially degrades the improvement in constraining lithospheric structure that can be obtained by full wavefield migration of *S*-to-*P* scattered/converted energy (Rondenay *et al.* 2005). Therefore, CCP stacking of *S*-to-*P* RFs (Dueker & Sheehan 1997; Wittlinger *et al.* 2004) has become—and is likely to remain—a widely used tool for studying lithospheric structure. The goal of this paper is to quantify how laterally varying structure in the mantle lithosphere affects *Sp* waveforms and images of lithospheric structure constructed via CCP stacking.

2 METHODS

Our goal is to explore the finite-frequency sensitivity of *S*-to-*P* converted waves to the topography of sub-Moho velocity discontinuities. Therefore, we simulate wave propagation through two families of candidate 2-D Earth structures using the spectral element method, which is capable of fully accounting for the effects of lateral heterogeneity on the wavefield, including such phenomena as diffraction, wavefront healing, single- and multiple scattering (e.g. Komatitsch & Tromp 2002). We use the SPECFEM2D package (Komatitsch & Vilotte 1998) available from www.geodynamics.org to simulate the propagation of an input planar displacement shear wavefield for four different ray parameters ranging from 0.1002 to 0.1207 s km⁻¹. A total of 8 simulations are carried out for each candidate Earth structure, representing four sources at the surface and epicentral distances of 55° to 75°, coming from the left and right sides of the model. When the candidate Earth structure is symmetric with respect to reflection across the depth-axis, the wavefields coming from the left and right interact with the structure in identical ways, in which case only four simulations are carried out.

We construct 16 symmetric and 13 asymmetric candidate structures, illustrated schematically in Fig. 1. These models allow us to systematically explore the effects of the following variables on the *Sp* RFs and resulting single-station and CCP stacks:

- (i) Depth of the velocity interface, placed at 65, 85, 105, 125, 145 km;
- (ii) Slope of the topography on the interface in the asymmetric models (top panel, Fig. 1), set at 7.0°, 14.0°, 26.5°, 45.0° or 63.4°,

corresponding to rise-over-run (tangent) values of 1/8, 1/4, 1/2, 1 and 2;

(iii) Lateral extent (width) of lithospheric protrusions and indentations (bottom panel, Fig. 1), varied between 48, 112, 144 and 208 km.

(iv) Spacing of stations at which the wavefield is recorded, set at 10, 20, 40 or 80 km;

(v) Illumination geometry;

(vi) Frequency content of the wavefield, with power between 0.03 and 0.25 Hz and 0.03 and 0.125 Hz;

(vii) Taper applied to the observed *P* and *SV* waveforms;

(viii) Deconvolution method.

For each simulation, the recorded vertical and horizontal waveforms are integrated to displacement (so that the incoming particle motion is a single Gaussian), then a third-order polynomial fit is removed to eliminate long period artefacts. The waveforms are filtered using an eighth-order, zero-phase, Butterworth bandpass filter. Because the input *S* wavefield contains higher frequencies than those typically present in actual data, the 0.03–0.25 Hz passband yields waveforms with a 4 s dominant period, which is higher than the 8–12 s dominant period typically present in actual data filtered with the same passband. Therefore, the 0.03–0.125 Hz passband yields waveforms with frequency content more similar to those typically observed in actual *Sp* recordings.

The filtered waveforms are then transformed to the incoming *P*–*SV* wavefield using the free-surface transform matrix, which, though strictly valid only for an isotropic half-space (Kennett & Engdahl 1991), is routinely used to separate the *P* and *SV* energy. The *S* arrival time (t_s) is picked at the largest amplitude arrival in the *SV* trace, and both the *SV* and *P* traces are then windowed with a cosine taper that removes signal at $t < t_s - 50$ s and either $t > t_s$ or $t > t_s + 15$ s. The period of the cosine taper is set to equal the inverse of the higher corner frequency of the bandpass filter applied to the data $f_h = 0.25, 0.125$ Hz. The two taper positions are used in order to investigate the significance of including and not including post *SV*-arriving energy in the deconvolution when constructing *Sp* RFs. The resulting *SV* trace is then deconvolved from the *P* trace by three common deconvolution techniques: (1) individual damped frequency domain deconvolution (IFDD; e.g. Bostock 1998); (2) iterative time domain deconvolution (ITDD; Ligorria & Ammon 1999); (3) extended time multi-taper method (ETMTM; Park & Levin 2000; Helffrich 2006; Shibutani *et al.* 2008) as implemented by Lekić & Fischer (2014). The deconvolved trace is the single source to single station RF.

Damping is added to the denominator of the spectral division in both IFDD and ETMTM deconvolution, and has the effect of both reducing the amplitude of the retrieved RF and enhancing its long period character. We partially compensate for the amplitude reduction using the correction proposed by Ammon (1991). While there is no consensus concerning the optimal way of choosing the amount of IFDD damping, the typical approach is to increase damping until spurious oscillations arising from frequencies at which the denominator is near zero are suppressed. In this study, we choose the IFDD damping level at which the variance of the resulting RF trace changes most as the damping level is incrementally changed; this damping level can be automatically found by searching across different damping levels and has the advantage of avoiding both damping levels too small to affect the RFs and damping levels so large that they dominate the deconvolution. As described in the supplement of Lekić & Fischer (2014), the damping used in the ETMTM is chosen to minimize the sum of the L-1 norm of the RF

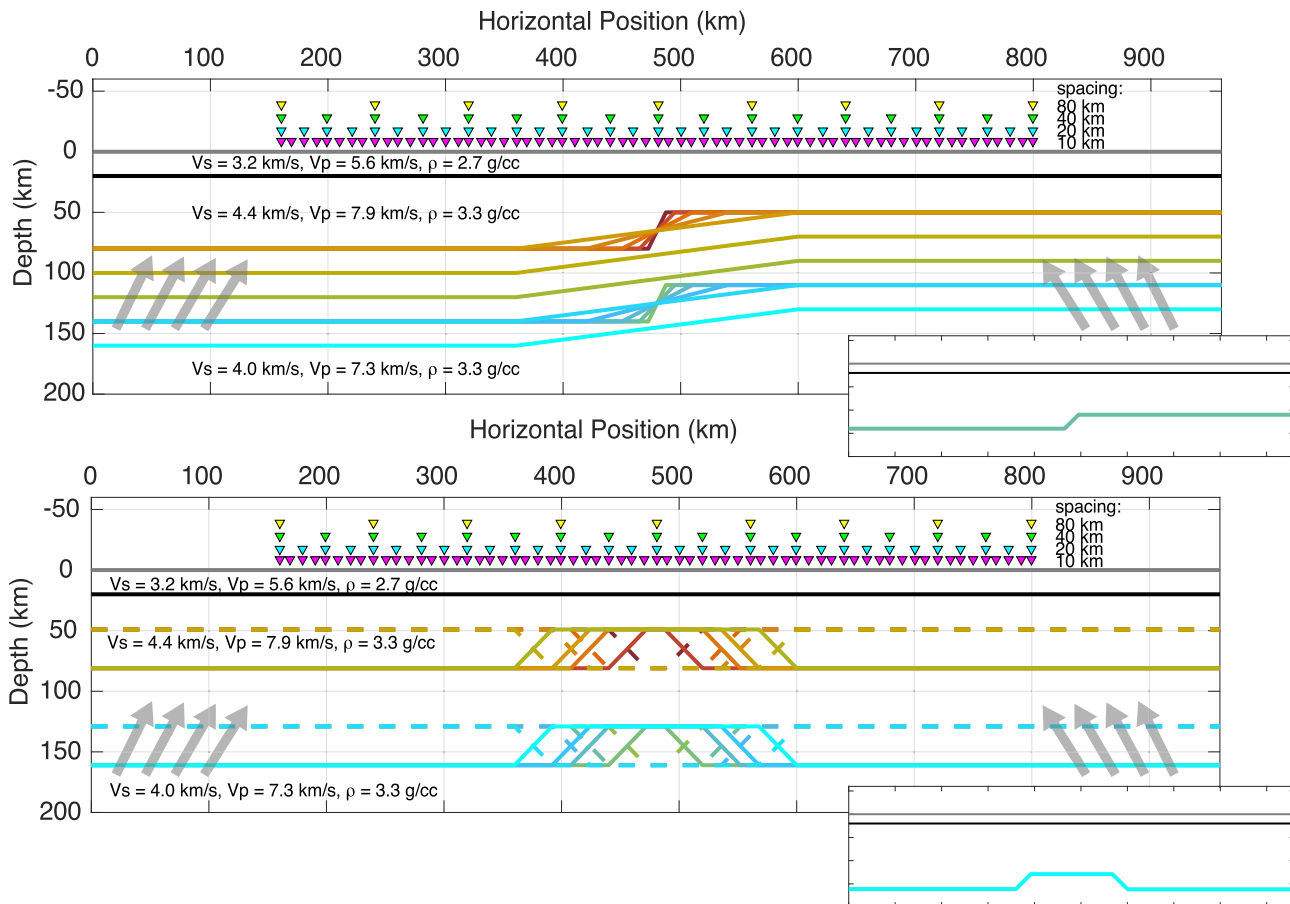


Figure 1. Schematic representation of input models and illumination geometries. Crustal thickness is 20 km across our model section, and crustal V_p is 5.6 km s^{-1} and V_s is 3.2 km s^{-1} . Mantle lithospheric thickness varies from 16 km thinner to 16 km thicker than the mean LAB depth, which is varied between 65° and 150° . The slope of the LAB topography is varied between 7° and 64° . The arrows indicate the approximate propagation direction of the incoming S wavefields (corresponding to four ray parameters spanning typical S_p epicentral distances), which enters the model space from the left or the right. The magenta triangles denote the positions of the 80 receivers at which the wavefield is recorded. The insets illustrate example asymmetric (top) and symmetric (bottom) models.

and the L-1 misfit between the P trace and that predicted by the convolution of RF with the SV trace. In the ITDD method, Gaussians with a half-width of 2 s are iteratively added to model the RF, and the number of iterations is set *a priori*; we set it to 100. The RF is then mapped from time to depth using the known crustal and lithospheric mantle velocities. Once an RF in depth is obtained for all the sources recorded by a station, these can be averaged to yield the common station stack.

CCP stacks are constructed following Lekić *et al.* (2011). We take individual single station RFs, and project them into the physical area (vertical section) defined by depth (z) and horizontal distance (x) using 1-D ray tracing along the direction of incidence and ray parameter of the parent S phase and the average velocity profile with depth calculated by horizontally averaging the model used for computing the synthetics. The physical model area is discretized every 1 km, and at each discrete location (x_k, z_k), the CCP stack is the weighted average of all RFs at that depth, where the weighting factor $\gamma(d)$ is given by

$$\gamma(d) = \begin{cases} \frac{3}{4}\hat{d}^3 - \frac{3}{2}\hat{d}^2 + 1, & \text{for } \hat{d} \leq 1 & (1) \\ \frac{1}{4}(2 - \hat{d})^3, & \text{for } 1 < \hat{d} \leq 2 & (2) \\ 0, & \text{otherwise} & (3) \end{cases}$$

where $\hat{d} = d/d_0$, and d is the horizontal distance between the location of the back-traced ray at a given depth and the discrete locations at which the CCP stack is computed at that same depth.

In order to physically relate this weighting function $\gamma(d)$ to the smoothing of structure inherent to the wavefield, we draw an analogy between it and the zero-offset Fresnel zone half-width $2d_0$, and therefore parametrize $\gamma(d)$ in terms of depth z_k and converted-wave (P) wavelength λ :

$$d_0 = \frac{1}{2} \sqrt{\left(\frac{\lambda}{2} + z_k\right)^2 - z_k^2}, \quad (4)$$

where λ is calculated for the high-frequency corner of the bandpass filter applied to the data.

Fig. 2 shows how the zero-offset Fresnel zone and the weighting function γ vary with ray parameter, period and depth (z) compared to the actual Fresnel zone as defined in Kvasnička & Vlastislav (1996), and an approximate Fresnel zone half-width given by $d_F = \sqrt{\frac{z\lambda}{\cos^3(\theta_P)}}$ (e.g. Wittlinger & Farra 2007), where θ_P is the emerging angle of the P wave, which can be derived from the exact Fresnel zone expressions by neglecting a term of order λ^2 . The half-width is defined in the horizontal plane. We can see that the zero-offset Fresnel zone half-width ($2d_0$, dashed line) is the lower limit on the half-width of the actual Fresnel zone (red), which increases as a function of

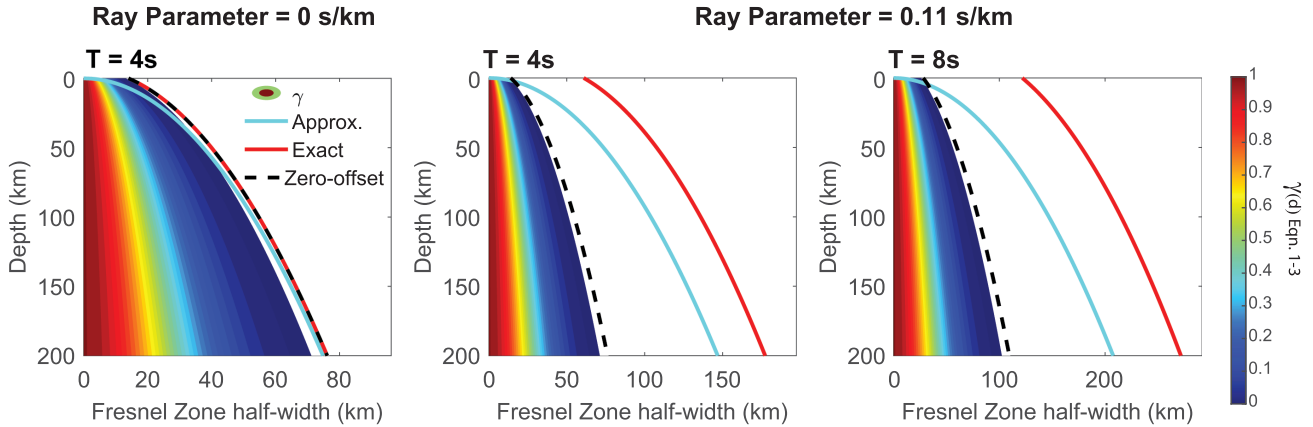


Figure 2. Comparison of the exact Fresnel zone half-width (red), Fresnel zone half-width approximation discussed in the text (cyan), zero-offset Fresnel zone half-width (dashed) and the weighting factors γ (contours) for computing the contribution of a receiver function at a particular horizontal distance to the common conversion point stack at a particular depth, computed for a period of 4 s and vertical incidence (left), and for a more typical Sp incident angle at 4 s (middle) and 8 s (right) period. The CCP smoothing lengthscale is always smaller than the Fresnel zone half-widths, so that potential sub-Fresnel zone scale features are less smoothed away in the CCP stacking procedure.

the ray parameter (incidence angle) and wavelength of the converted (in our case, P) wave (Kvasnička & Vlastislav 1996). The approximate Fresnel zone expression, on the other hand, is systematically smaller than the exact Fresnel zone, particularly at shallow depths, where λ and z are comparable. Fig. 2 illustrates the two reasons we use the zero-offset instead of the actual Fresnel zone half-width in defining our weighting function γ for CCP stacking: (1) Since it does not depend on the ray parameter of the incident wavefield, it can be uniquely defined for a specific wavefield frequency content and CCP location and, (2) it is always smaller than the true Fresnel zone, reducing the possibility of smoothing away sub-Fresnel zone structures, insofar as their signature is present in the Sp wavefield.

3 RESULTS

To systematically map out and understand the effects of the parameters investigated on the Sp wavefield, RFs and CCP stacks, we have analysed 84 Sp wavefields (each recorded by up to 65 stations), 252 sets of RFs, and over 1000 different CCP stacks. In this section, we present a small subset of figures that summarize our main findings.

3.1 Asymmetric models

We begin by considering the simplest possible asymmetric 2-D geometry: a LAB-type velocity interface (i.e. velocity and impedance drop of 8 per cent with depth) which transitions from depth $z - 16$ km to depth $z + 16$ km over a width W ranging from 4 to 128 km. Due to the asymmetry of the structure, the illumination from the left (thick lithosphere) and the right (thin lithosphere) of the model by teleseismic S waves is treated separately.

Velocity Sp waveforms on the P component, filtered from 0.03 to 0.25 Hz (dominant period of 4 s), for different asymmetric model and illumination geometries are shown in Fig. 3 for receivers spaced 10 km apart. The behaviour of waveforms with more realistic frequency content typical of some Sp studies (i.e. dominant period of 8 s) is qualitatively the same, but less instructive for illustrating the behaviour of the Sp wavefield. Two arrivals are generally visible on the P component: an arrival from the Sp conversion across the Moho (red), which can be seen ~ 4 s before the main S arrival; and

arrival(s) from the Sp conversion across the LAB (blue), which can be seen to precede the Moho conversion, at times proportional to the depth of the LAB.

When illumination is from the side with thinner lithosphere (Fig. 3, right panels), and LAB topography is gently sloped (7° , Fig. 3, bottom row), a clear Sp conversion generated across the LAB can be traced across all receivers. As LAB topography steepens to 14° , a secondary Sp arrives after the main LAB-related Sp phase (purple arrows in Fig. 3), which might be misinterpreted as a conversion across a shallower LAB depth that is not in fact present in the input model. At steeper topographies, the Sp conversion no longer appears to transition smoothly from deep to shallow LAB depths, and the secondary Sp phase gives the appearance of a double velocity interface. Furthermore, a pronounced Sp phase opposite in polarity to that arising across the LAB can be seen at a number of stations (orange arrows in Fig 3).

When illumination is from the side with thicker lithosphere (Fig. 3, left panels), the waveforms of Sp behave differently. The Sp conversion across the LAB cannot be traced from deeper to shallower LAB when the slope on the LAB is steeper than 7° (Fig. 3, bottom row). If the incoming wavefield has a larger ray parameter (closer epicentral distance), then even the 7° topography cannot be smoothly traced in the waveforms. Instead, the Sp conversions consistent with both the thinned and thickened lithosphere are seen to overlap (green arrows in Fig 3) giving the impression of a double velocity interface. The effect of steepening LAB topography is to extend the range of stations across which both LAB-related Sp phases are seen, extending in the example of Fig. 3 across stations spanning nearly 200 km in distance. Put differently, the Sp phases whose timing and polarity are consistent with the deeper LAB are clearly observed at all stations, whether or not they are underlain by thin or thick lithosphere. However, at stations underlain by thinner lithosphere, Sp phases consistent with the shallower LAB are also observed. A physical explanation for this behaviour is discussed in Section 4.1.

Because P and S waveforms manifest directly in Sp CCP stacks, the appearance of the stacks varies greatly depending on the direction of illumination and on the topography of the structure being imaged. In Fig. 4, we illustrate the effect of illumination direction on CCP stacks for three different topography slopes (63.4° —top row, 26.5° —middle row, and 7° —bottom row) and an on-average

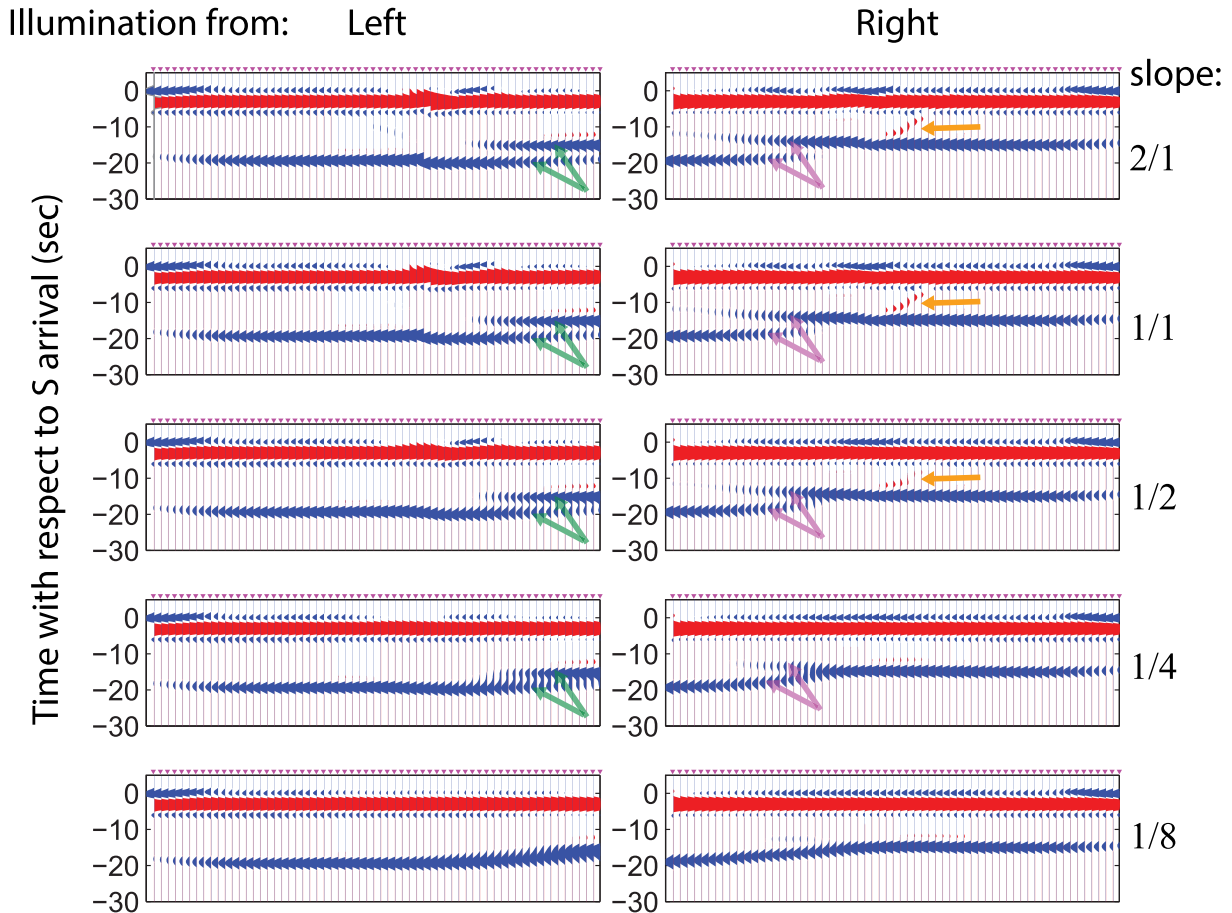


Figure 3. Sp waveforms (P component of motion), 0.25 Hz corner, ray parameter of 0.107 s km^{-1} , for illumination from the side with thicker lithosphere (left column) and thinner lithosphere (right column), average depth of 125 km, and topography slope of 7.0° (bottom row), 14.0° , 26.5° , 45.0° and 63.4° (top row), as illustrated in Fig. 1. Waveform amplitude is scaled by the maximum of the S and scaled by a factor of 4x. Sp converted across the Moho (red, positive arrival) is seen at -4 s , and conversions across shallower and deeper portions of the LAB (blue, negative arrival) are present at -15 and -20 s , respectively. Note the effect of illumination geometry on the waveforms: illumination from the thicker lithosphere side produces pronounced duplexing of the Sp conversions (green arrows) for but the most shallow-dipping of LAB topographies (7° slope), while illumination from the thinner lithosphere side has less prominent duplexing (purple arrows), yields opposite-polarity Sp arrivals following the direct converted phases (orange arrows), and retrieves the velocity interface with 26.5° slope.

125 km deep LAB. The CCP stacks are constructed using a 0.03–0.125 Hz passband, 10 km station spacing, and deconvolution using the extended time multitaper method (ETMTM). Illumination from the thicker lithosphere side (left) does not yield CCP stacks which faithfully resolve steep LAB topography. Instead, slopes steeper than 7° appear less steep in the CCP stack than they are in the input model. Illumination from the thinner lithosphere side (right), however, yields CCP stacks that retrieve the abruptness of the LAB depth transition. When the slope is steeper than 7° , the Sp conversion across the LAB is weak, resulting in reduced amplitudes in the CCP stacks.

When illumination is even from both sides of the asymmetric structure, a gently sloping LAB topography (7°) can be retrieved across the range of LAB average depths tested. This can be seen in Fig. 5, which shows Sp CCP stacks at three different depths (65 km—top, 105 km—middle, 145 km—bottom), a topography slope of 7° , a 0.03–0.125 Hz passband, and ETMTM deconvolution. The left column is for station spacing of 20 km, similar to that used in many large scale, temporary, broadband deployments (Gao *et al.* 2004), while the right column is for station spacing of 80 km, comparable to that used by the EarthScope Transportable Array in the lower 48 states. From this figure, and a series of related tests, we con-

clude that even an 80 km station spacing is sufficiently dense for retrieving gently sloped LAB topography across the range of relevant lithospheric depths. This finding confirms the utility of CCP stacking in the depth range where wavefield migration techniques would be expected to suffer from operator aliasing (Rondenay *et al.* 2005). However, we stress that this spacing is insufficient for Sp imaging of similarly sloping crustal structures, as suggested by aliasing in the retrieved Moho signal visible in the right panels of Fig. 5.

3.2 Symmetric models

In order to probe the effects of lateral extent of LAB topography, and compare the signatures of upward versus downward deflections of LAB topography on the Sp wavefield, we simulate wave propagation through a host of candidate symmetric structures, illustrated in Fig. 1. Crustal thickness is held constant at 20 km across each model, while a LAB at either 65 km or 146 km depth is made 32 km deeper or shallower within a region whose width is set to either 48, 112, 144 or 208 km. The results of this analysis are presented in Figs 6 and 7. Because the structures investigated are symmetric with respect to reflection in the vertical axis, wavefield interaction with

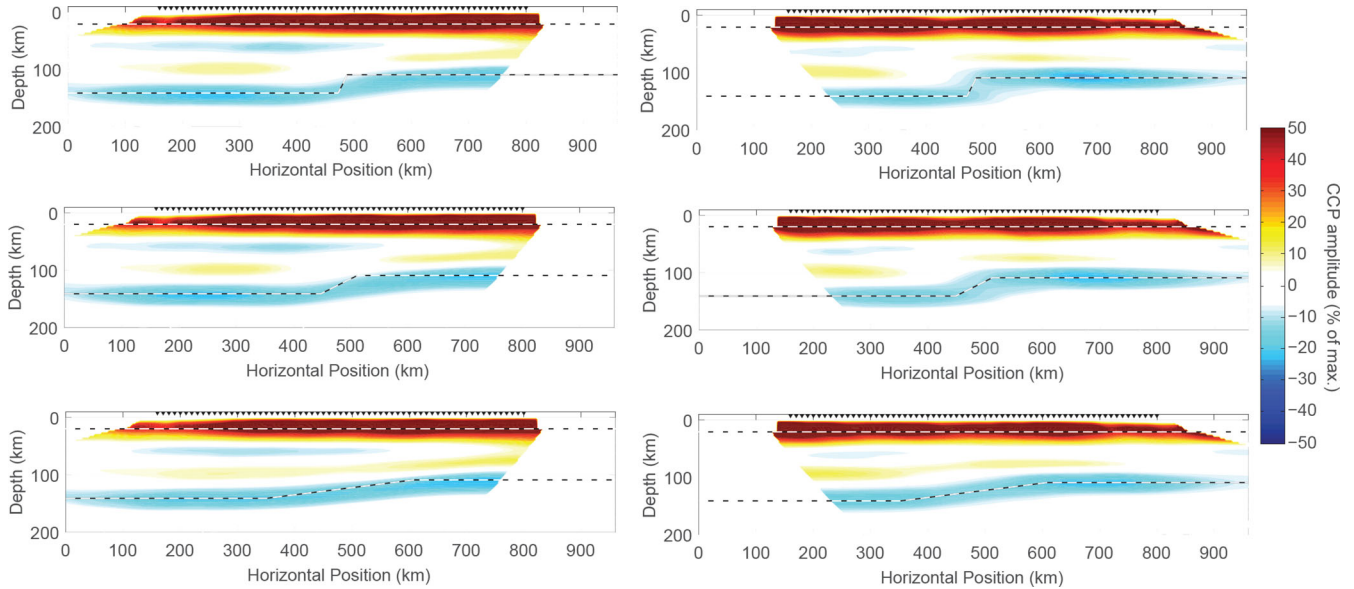


Figure 4. Effect of illumination direction on common conversion point stacks for different topography slopes (63.4° —top row, 26.5° —middle row and 7° —bottom row), a 125 km deep LAB, 0.03–0.125 Hz passband, 10 km station spacing and ETMTM deconvolution. Illumination from the thicker lithosphere side (left) is not conducive to imaging steep LAB topography and slopes steeper than 7° appear shallower in the CCP stack than they are in the input model. This is because *S*-to-*P* waves diffracting from the deep corner (see Fig. 8) are mapped into a spurious, gently sloped topography. Illumination from the thinner lithosphere side (right), however, yields CCP stacks that retrieve the abruptness of the LAB depth transition. When the slope is steeper than 7° , the *Sp* conversion across the LAB is weak, resulting in reduced amplitudes in the CCP stacks. On this and all other CCP figures, the colour scale saturates at 1/2 of the maximum absolute value of the stack.

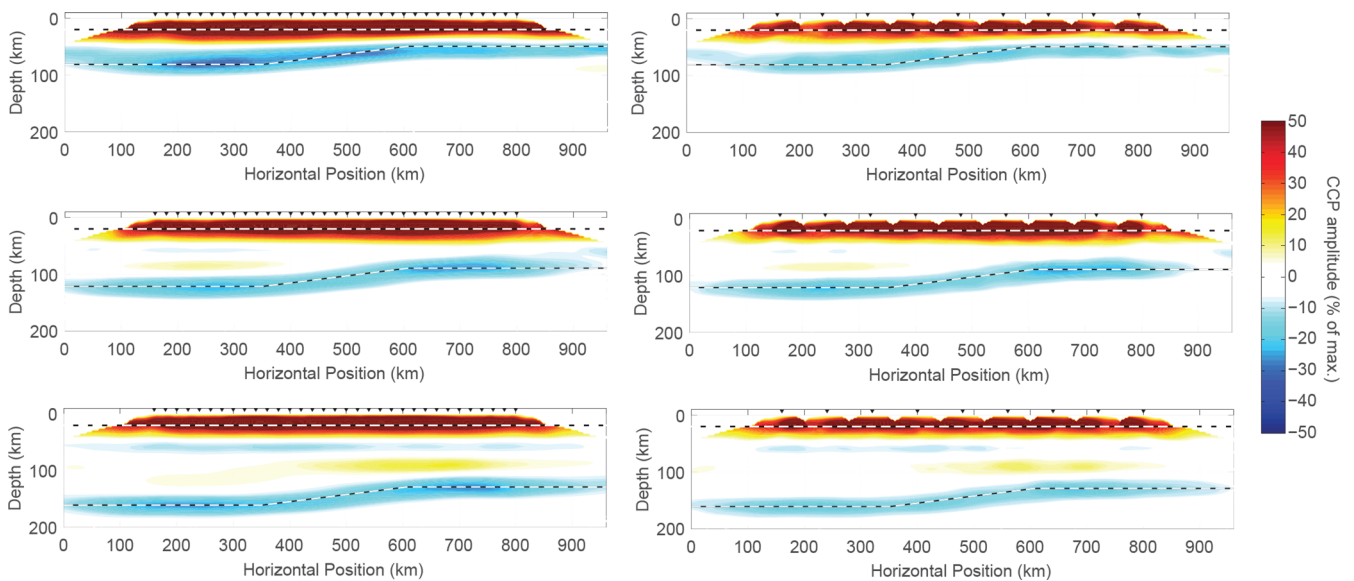


Figure 5. Effect of station spacing on the common conversion point stacks at three different depths (65 km—top, 105 km—middle, 145 km—bottom), a topography slope of 7° , illumination from both sides, a 0.03–0.125 Hz passband and ETMTM deconvolution. Both a 20 km (left) and 80 km (right) station spacing is sufficient for retrieving gently sloped LAB topography across this range of depths. Aliasing in the retrieved Moho signal with a station spacing of 80 km suggests that this station spacing—comparable to that of the EarthScope Transportable Array—is insufficient for *Sp* imaging of shallower structure.

the structure is identical regardless of the illumination direction. However, we document a pronounced asymmetry of the effect of lithospheric thickening compared to thinning on the *Sp* waveforms.

To illustrate this effect, we plot *Sp* CCP stacks with illumination from both sides, with a 0.03–0.125 Hz passband, 10 km station spacing, ETMTM deconvolution, LAB depth of 145 km, and widths of 48 km (top), 112 km, 144 km and 208 km (bottom) in Fig. 6. While lithospheric thickening across 208 km (bottom right) can be unequivocally recognized in the CCP stacks, the signature of

an analogous lithospheric thinning (bottom left) is muted both in depth and lateral extent. Similarly, while a 144 km wide thickening notably affects the signature of the LAB *Sp* conversion, an analogous thinning does not. This difference in behaviour can be understood to result from the duplexed/overlapping *Sp* phases first seen in Fig. 3, which combine across stations and wavefields (with different ray parameters) to extend the apparent lateral extent of the LAB in a way that ‘fills in’ regions of thinned lithosphere while extending the apparent width of thickened regions.

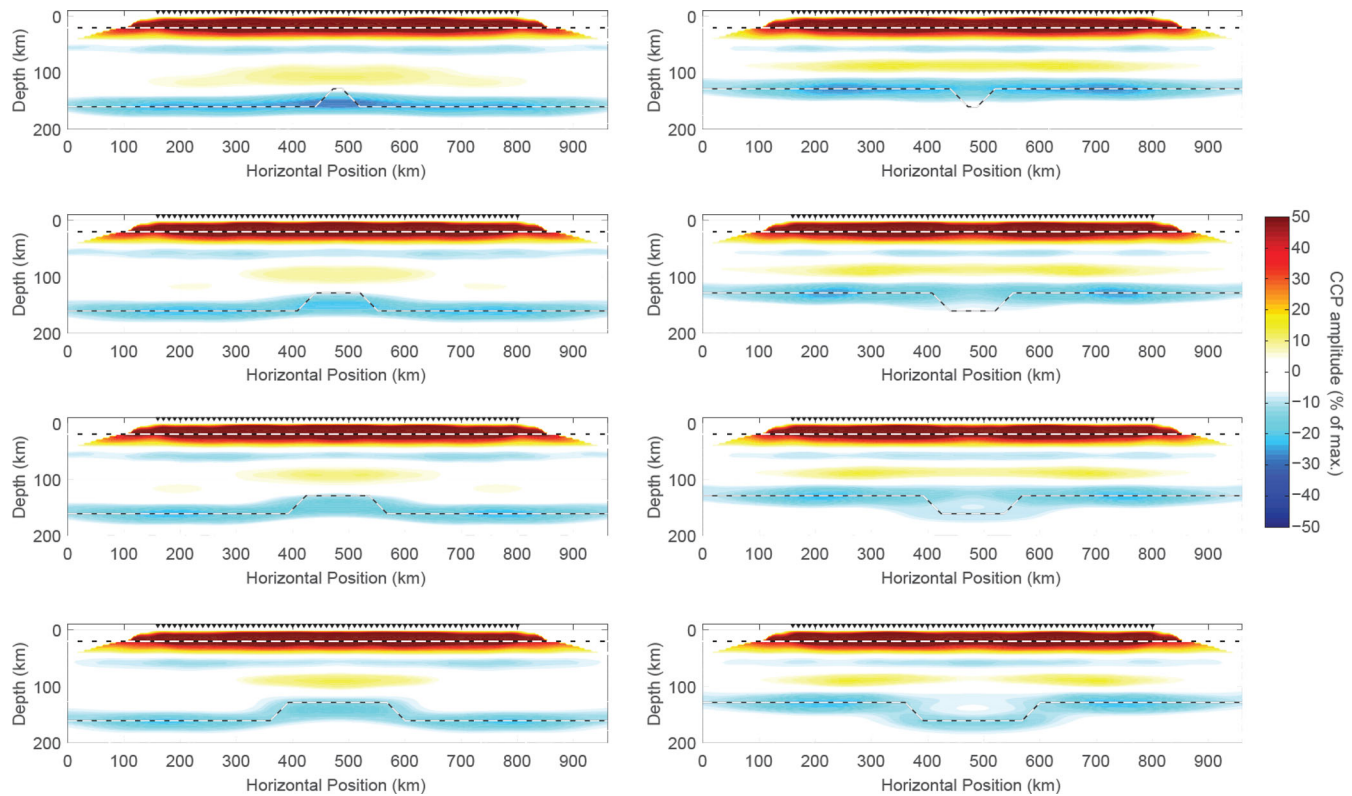


Figure 6. Asymmetry of the effect of lithospheric thickening (right) compared to thinning (left) in a symmetric model with illumination from both sides, with a 0.03–0.125 Hz passband, 10 km station spacing, ETMTM deconvolution, LAB depth of 145 km and widths of 48 km (top), 112 km, 144 km and 208 km (bottom). While lithospheric thickening across 208 km (bottom right) can be unequivocally recognized in the common conversion point (CCP) stacks, the signature of an analogous lithospheric thinning (bottom left) is muted both in depth and lateral extent. Similarly, while a 144 km wide thickening notably affects the signature of the LAB Sp conversion, the analogous thinning does not. This difference in behaviour can be understood as the combined signature of multiple corner diffractions, which combine to extend the apparent lateral extent of the LAB in a way that ‘fills in’ thinnings while extending the apparent width of thickenings. Note the prominent, reverse-polarity signals overlying the LAB. These are not manifestations of actual intralithospheric structure or layering. Instead, they are manifestations of the *S*-to-*P* corner diffractions produced by illumination from the side with thinner lithosphere (see Figs 3 and 8). Therefore, when illumination is not from both sides of the LAB topography structure, the reverse polarity signals would not be present on both sides of the structure and would manifest themselves differently for thickened versus thinned structures. When illumination is from the left (right) for the lithospheric thinning, the reverse polarity signals would be apparent on the right (left) portion of the CCP stack. When illumination is from the left (right) for the lithospheric thickening scenario, the reverse polarity signals would be apparent on the left (right) of the CCP stack.

We determine that neither an upward nor downward deflection that extends across 48 km width is directly resolvable in the Sp CCP stacks, regardless of whether a 0.25 Hz or 0.125 Hz upper corner is applied to the synthetics. Therefore, the method should not be used when targeting structures of very small lateral extent, even when higher-than-typical frequency content is present in the Sp wavefield. Even a 112 km wide region of thickened lithosphere only slightly weakens the amplitude of the LAB imaged in the CCP stacks, while a 112 km wide region of thinned lithosphere has an even lesser signature. The situation is not much better when the LAB is shallower, as shown in Fig. 7, which shows the Sp CCP stacks for a LAB at 65 km depth and lithospheric thinning and thickening over a distance of 112 km (upper panels) and 208 km (lower panels). Stacks constructed using Sp waveforms filtered in the 0.03–0.125 Hz passband—which, as mentioned previously, yield Sp wavefields with frequency content more commonly found in observational studies—are unable to resolve the 112 km wide lithospheric thickness perturbations, and only partially resolve the 208 km wide ones. Thus, retrieval of these downward and upward deflected structures is actually worse at shallower depths. The situation substantially improves when higher frequency Sp waves (0.03–0.25 Hz passband) are used, yielding CCP stacks that reveal

the thinned and thickened structure of both the 112 and 208 km lateral extent. However, the 112 km wide lithospheric undulations (particularly the thinning) is characterized by a double LAB-like phase, which is a manifestation of the duplexing seen before (e.g. Fig. 3) that also appears prominent in the higher frequency passband.

The vertical and lateral resolution of Sp CCP stacks has been discussed in previous studies (e.g. Wittlinger & Farra 2007; Rondenay 2009), and is directly related to the converted-wave wavelength and Fresnel zone width at the depth of interest, respectively. Though based on sound theoretical principles (Kvasnička & Vlastislav 1996), this framework for estimating the resolving power of Sp studies appears to be incomplete, because it predicts some, but not all of the behaviours seen in Fig. 7. For example, Fresnel zone width decreases at higher frequencies (see Fig. 2), which is consistent with the improved resolution of the CCP stacks constructed with higher frequency Sp waves (compare left and right panels of Fig. 7). However, Fresnel zone width also decreases with decreasing depth (see Fig. 2), yet the ability to retrieve lithospheric thickness perturbations in the CCP stacks appears to degrade at shallower depths (compare bottom right panel of Fig. 6 with the bottom right panel of Fig. 7). Furthermore, the horizontal extent of discontinuity

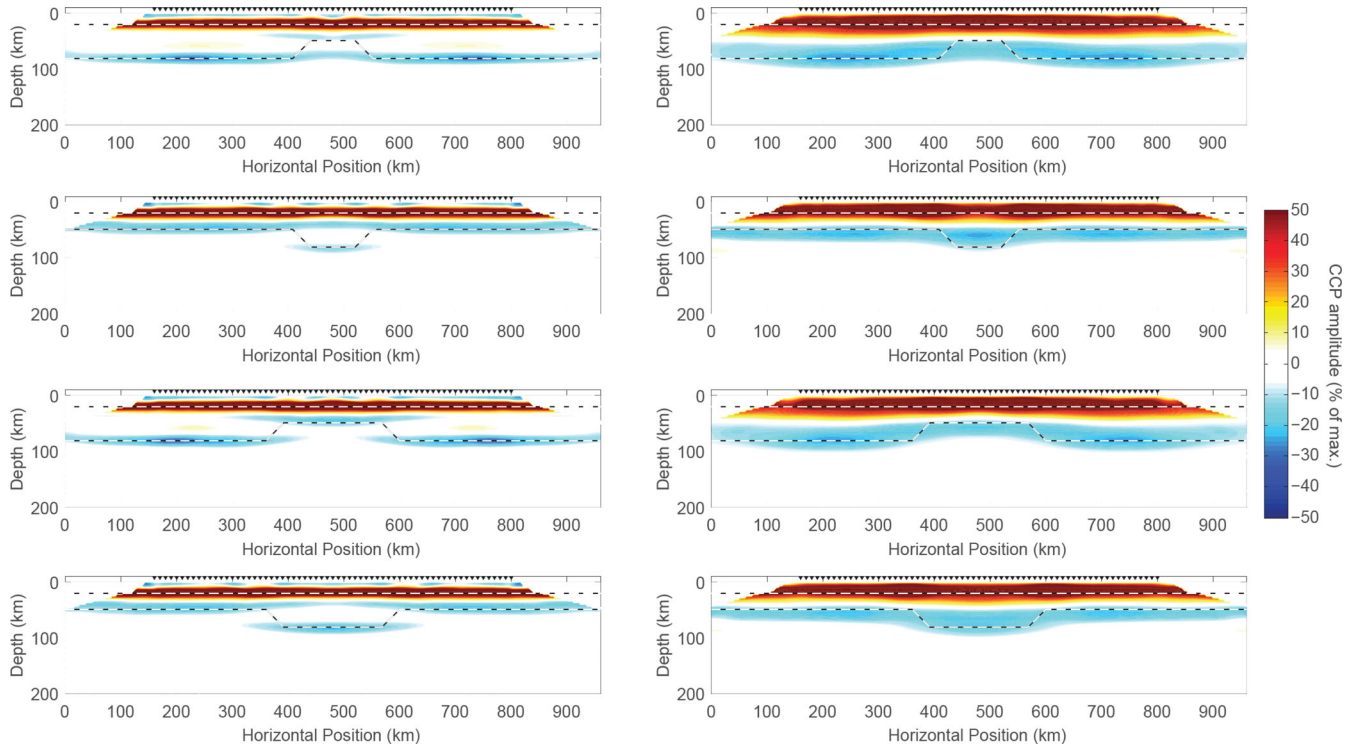


Figure 7. Effect of wavefield frequency content on common conversion point stacks for 10 km station spacing, a LAB at 65 km depth, and lithospheric thinning and thickening over a distance of 112 km (upper panels) and 208 km (lower panels). Deconvolution is accomplished using the ETMTM. Higher frequency Sp waves (0.03–0.25 Hz passband) yield CCP stacks which reveal the thinned and thickened structure of both sizes, while lower frequency waves (a more realistic 0.03–0.125 Hz passband) are unable to resolve the 112 km wide thickness perturbation and only partially resolve the 208 km wide ones. Note that the *S*-to-*P* corner diffractions are prominent in the higher frequency passband and result in a duplexed Sp CCP stack for both 112 km wide structures.

depth variations that can be seen in the CCP stacks shown in Figs 4, 6 and 7 appear to be smaller than the half-width of the Fresnel zone. For example, the Fresnel zone half-width (red line in Fig. 2) is ~ 250 km for 8 s waves at ~ 150 km depth, yet a 208 km wide lithospheric thickening is clearly resolved in Fig. 6, while even a 144 km thickening produces a clear disruption in the interface seen in the CCP stacks.

The ability to image—under some circumstances—structures smaller than the Fresnel zone half width is not altogether surprising. For example, sub-Fresnel zone sensitivity has been observed for shear-wave splitting measurements (e.g. Alsina & Snieder 1995) and core-reflected waves (e.g. Shearer 1991). Using a 2-D numerical experiment, Spetzler & Snieder (2001) showed that a plane wave directly incident on slowness perturbations smaller than the Fresnel zone width experiences systematic and analysable traveltime variations (see their fig. 4). More recently, Deng & Zhao (2015) computed RF topography sensitivity kernels accounting for finite-frequency effects and showed that even sub-Fresnel zone topography variations produce observable signals (their figs 11 and 12), and that the kernels they computed also exhibit sub-Fresnel zone scale structure (their figs 18 and 20). Our results are consistent with these studies, but additionally illustrate that waveform complexity—as exhibited in Sp conversion duplexing and opposite-polarity arrivals seen in Fig. 3—appears to be partly responsible for degrading the resolution of CCP stacks compared to expectations based on Fresnel zone analysis. We conclude that Fresnel zone arguments might, in some cases, underestimate the true resolution, and in other cases, represent best-case scenarios appropriate for situations in which abrupt lateral variations in structure do not yield waveform complexities.

4 DISCUSSION

4.1 Sp waveform complexity

The duplexed Sp phases seen in Fig. 3 have profound implications for interpreting Sp RFs and CCP stacks. In part, this is because they can be misinterpreted as multiple intralithospheric velocity interfaces. Additionally, these phases are related to the asymmetric appearance of structures illuminated from different sides, as well as the asymmetry in the Sp signature (and appearance in CCP stacks) of localized lithospheric thickening versus thinning. Determining the origin of the duplexed Sp phases is, therefore, important for understanding the behaviours noted above.

In Fig. 8, we show Sp waveforms, filtered from 0.03–0.25 Hz, for a station spacing of 10 km, average LAB depth of 125 km, topography slope of 45° (rise-over-run of 1/1), and incoming S plane waves with two different ray parameters: 0.1002 s km^{-1} (top) and 0.1207 s km^{-1} (bottom). We compute the expected arrival times of *S*-to-*P* conversions diffracted at the corners in the LAB topography by using Snell's Law and determining the scattering angle that would result in the *S*-to-*P* diffraction being recorded at each of the stations. These expected arrival times are shown in green and yellow solid lines, which can be seen to (approximately) overlie much of the complexity in the Sp converted phases. Expected arrival times of *S*-to-*S* corner diffractions are denoted by dashed lines, and occur at or after the Moho conversion. Therefore, unlike *S*-to-*P* corner diffractions, *S*-to-*S* diffractions are unlikely to complicate interpretations of Sp RFs because they do not arrive at times consistent with Sp conversions across intralithospheric layering. Based on this kind of analysis performed on the range of synthetic wavefields, we

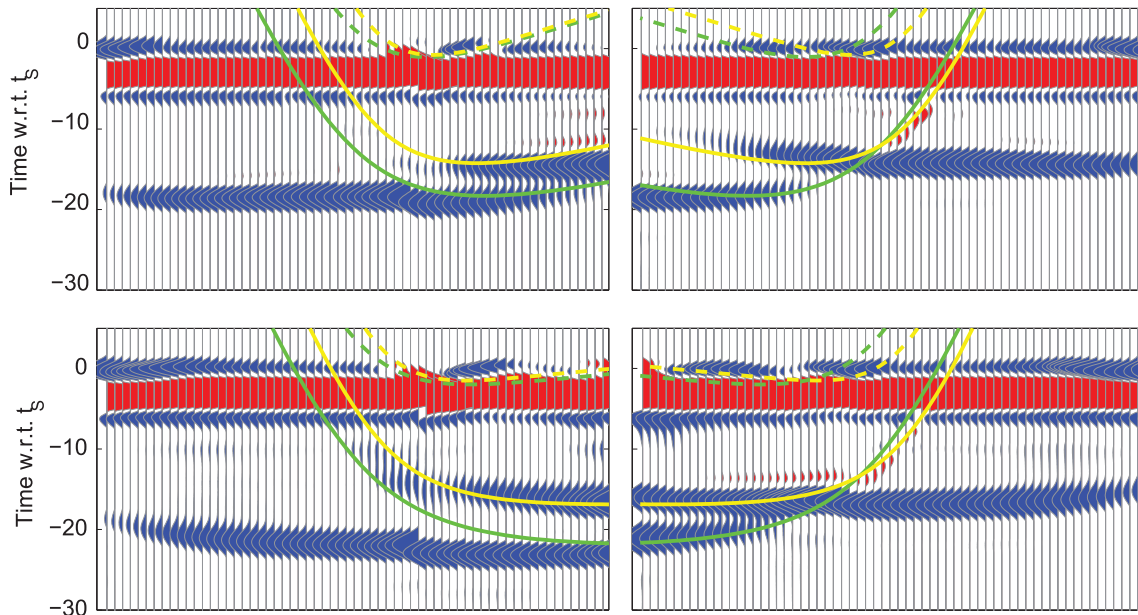


Figure 8. Sp waveforms, 0.25 Hz corner, for illumination from the side with thicker/thinner lithosphere (left/right), average LAB depth of 125 km, topography slope of 45° (rise-over-run of 1/1), and two ray parameters: 0.1002 s km^{-1} (top) and 0.1207 s km^{-1} (bottom). Positive arrivals are coloured red and negative ones blue, where the sign convention is such that positive corresponds to an Sp conversion across a velocity increase with increasing depth. Expected arrival times of S-to-P conversion and diffraction at the corners in the LAB topography shown in green and yellow solid lines. Much of the complexity in the Sp converted phases can be explained by corner diffractions, which can be misidentified as the LAB or intralithospheric discontinuities. S-to-S corner diffractions (dashed lines) arrive at or after the Moho conversion and are unlikely to complicate interpretations of Sp receiver functions. Note that the amplitude and moveout of the diffracted waves depend strongly on ray parameter of the incident wavefield, and that illumination from the thinner lithosphere side can produce prominent S-to-P diffractions opposite in polarity to those related to the flat LAB, which can also be seen in the right panels of Fig. 3.

conclude that the duplexed Sp phases arise due to diffraction of S-to-P converted waves produced at corners where the slope of LAB topography changes abruptly. Depending on the illumination direction and ray parameter, the moveout of the S-to-P waves diffracting from the deep corner can differ dramatically, giving rise to both spurious, gently sloped topography (as seen in the left panels of Figs 4 and 7) as well as unphysical, steeply dipping structures within the lithosphere (right panel of Fig. 3).

Note that, just like the moveout, the amplitude of the corner diffracted S-to-P waves depends strongly on ray parameter of the incident wavefield. Indeed, illumination from the thinner lithosphere side (right panels of Fig. 8) can produce prominent S-to-P diffractions opposite in polarity to those related to the flat LAB, which can also be seen in the right panels of Fig. 3. These prominent, reverse-polarity signals can constructively stack in the CCPs to produce a spurious structure that would suggest the presence of an impedance jump with increasing depth above the LAB. This can be seen in the right panels of Fig. 4 and the bottom panels of Fig. 5, at about the 600 km along the CCP cross-sections.

In Fig. 6, the manifestations of this spurious intralithospheric layering appear as dipping impedance jumps with depth symmetrically arranged across the CCP section. Because the excitation of the reverse polarity S-to-P corner diffractions is more efficient when illuminated from the side with thinner lithosphere (see Figs 3 and 8), the artefacts only appear symmetric in the CCP stack because illumination is from both sides. Indeed, when illumination is not equal from both sides of the LAB topography structure – a circumstance often encountered in Sp imaging – the reverse polarity signals would not be present on both sides of the structure and would manifest themselves differently for thickened versus thinned structures. When illumination is from the left (right) for the lithospheric thinning, the reverse polarity signals would be

apparent on the right (left) portion of the CCP stack. When illumination is from the left (right) for the lithospheric thickening scenario, the reverse polarity signals would be apparent on the left (right) of the CCP stack. Interestingly, their prominence even for LAB undulations of small lateral extent suggests that the presence of such apparent ‘intralithospheric’ structures might provide a means of indirectly inferring the presence of small scale LAB variations.

4.2 Windowing and deconvolution

A number of deconvolution methods are commonly employed in Sp imaging in order to reduce signal complexity due to the source time function and source side structure. In Fig. 9, we illustrate the differences in RFs obtained with ITDD (top row), IFDD (middle row) and ETMTM (bottom row) deconvolution (see Section 2) for two different frequency passbands, and for different choices of the parent phase (S) window used in the deconvolution. Fig. 9 shows Sp RFs computed from a wavefield produced by the interaction of an incoming planar wavefront with ray parameter of 0.1002 s km^{-1} impinging from the left on an 145 km deep LAB thinned across 208 km, and the deconvolution damping parameters are chosen according to the criteria described in Section 2.

By comparing the left and middle columns of Fig. 9, we can understand the influence on the RFs of the frequency content of the incoming wavefield. RFs computed from waveforms filtered with a 0.03–0.25 Hz passband show clear duplexing of Sp phases in the region of thinned lithosphere, as well as a strong reverse-polarity diffraction. These RF features result from wavefield complexity arising from corner diffractions, and can be seen regardless of the

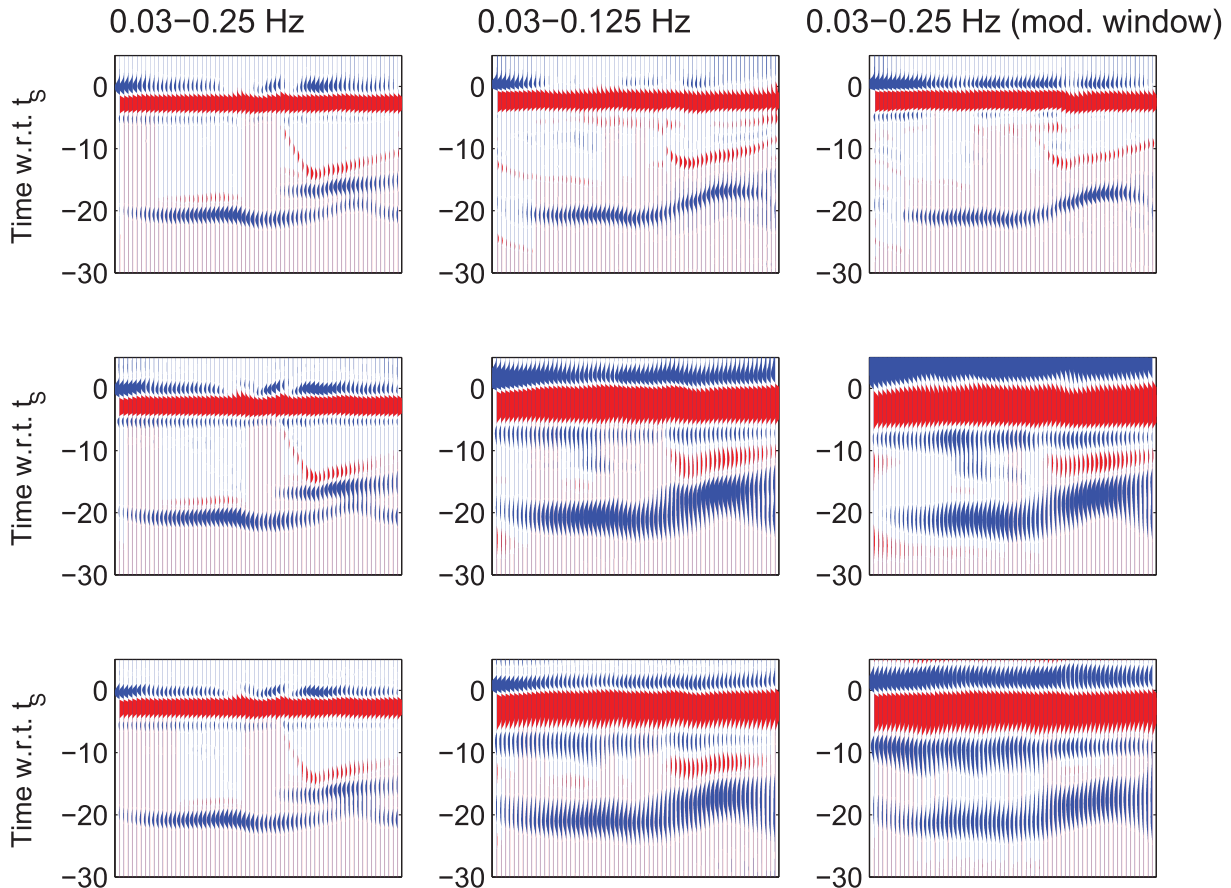


Figure 9. Effect of frequency content, deconvolution method and waveform windowing on S_p receiver functions (RFs). S_p RFs computed in the 0.03–0.25 Hz (left) and 0.03–0.125 Hz (middle and right) band, for illumination from the left, average LAB depth of 145 km, 208 km wide thinned lithospheric section (see Fig. 1), and ray parameter 0.1002 s km^{-1} . Deconvolution of S_p waveforms from the P waveforms is accomplished using iterative time domain (top), individual frequency domain (middle) and extended time multitaper method (bottom) deconvolution. Amplitudes are coloured the same way as in Fig. 8. The waveforms are windowed in the time domain before deconvolution to exclude post- S arrivals in the left and middle panels, but to include post- S arrivals in the set of panels on the right. Note the relative prominence of side-lobes in frequency-domain deconvolution, and the deleterious effects of not removing post- S arrivals on the RFs obtained using IFDD and ETMTM.

deconvolution method. Compared to ITDD RFs, both IFDD and ETMTM yield RFs that look somewhat longer period, as a result of the damping introduced to stabilize the spectral division. The middle column of Fig. 9 shows RFs for the longer-period 0.03–0.125 Hz passband (8 s dominant period typical of recorded S_p wavefields) which has less resolving power (see Fig. 7). The duplexed S_p phases are no longer seen in the thinned lithosphere region, regardless of the deconvolution method; nevertheless, their indirect effect of reducing the apparent slope of LAB topography is present. Furthermore, all three deconvolution methods yield RFs that have reverse-polarity corner diffractions, though these are most prominent in the ITDD results. Indeed, the ITDD and, to a lesser extent, the ETMTM RFs show more detail than RFs obtained with IFDD.

Differences among RFs obtained using three commonly used deconvolution methods suggest that more sophisticated approaches to removing the effects of source-side waveform complexity are likely to be worthwhile in improving the reliability of S_p RF inversions. Two promising approaches involve probabilistic deconvolution (e.g. Kolb & Lekić 2014) or direct modelling of the source-time functions (Dettmer *et al.* 2015).

In addition to the deconvolution technique and the frequency content of the incoming wavefield, RFs can be affected by the manner in which the parent (S) waveform is windowed. Waves reflecting from

the surface and internal interfaces arrive following the primary S wave; including or suppressing these arrivals in the waveform that is deconvolved from the P component can therefore affect the appearance of the RFs. In the left and middle panels of Fig. 9, and in all other RF figures in the manuscript, we applied a time-domain window on the input S and P waveforms (see Section 2) that tapers away waves arriving after the direct S before performing the deconvolution. In the right panels of Fig. 9, we compute RFs from wavefields filtered in the 0.03–0.125 Hz passband when the parent waveform windows include post- S arrivals. We find that windowing does not have a significant effect on the ITDD RFs, but use of the longer window has a notably and deleterious effect on the IFDD and ETMTM RFs. Comparing the middle and right columns of Fig. 9, we observe that while the ITDD RFs appear nearly identical, the longer parent phase window reduces the amplitude of the direct S_p conversions relative to the Moho side-lobes for the ETMTM and IFDD cases. Furthermore, arrivals related to the reverse-polarity corner-diffracted S_p are not visible in ETMTM RFs when the time-domain windowing does not taper away post- S arrivals. Based on these and similar analyses of other synthetic wavefields, we conclude that time-domain windowing to remove post- S arrivals before deconvolution yields more easily interpretable S_p RFs when frequency-domain methods (which include both IFDD and ETMTM) are used

for deconvolution, but that it is less important when time-domain deconvolution methods are used.

4.3 Implications of illumination geometry

Using synthetic modelling, we have documented that illumination geometry can substantially affect Sp CCP stacks, yielding different images of identical laterally varying structures illuminated from different sides and by incoming plane waves of different ray parameter. Analogous illumination effects have been documented in other imaging contexts, including reflection tomography (e.g. Burdick *et al.* 2013) and Ps imaging (e.g. Levander *et al.* 2005; Rondenay 2009). In order to illustrate the potential consequences of these effects, we consider two recent Sp studies and analyse their salient findings in the context of illumination geometry. We surmise that the dramatic lithospheric thinning imaged by Lekić *et al.* (2011) may be the result of fortuitous illumination geometry of the Salton Trough and the overall fairly shallow LAB in this region. This is because the orientation of the rift, and associated lithospheric thinning, is quasi-parallel to great circle paths trending north-westward back to the Aleutians, and south-eastward back to the South American subduction zone. On the other hand, when considered alongside the findings presented in this study, the failure to detect a clear signature of lithospheric thinning beneath the Rio Grande Rift (Lekić & Fischer 2014) does not necessarily mean that no lithospheric thinning occurs beneath this rift. This is because, unlike the Salton Trough, the axis of the Rio Grande Rift is not aligned with the dominant back-azimuths from which teleseismic S waves illuminate the LAB. This unfavourable geometry, together with the asymmetry that renders lithospheric thinning more difficult to identify than thickening from Sp CCP stacks (see Figs 6 and 7), might obscure lithospheric thinning that extends across horizontal distances of less than 200 km.

In this study, we analysed synthetic waveforms computed for four ray parameters that span the entire range usable in Sp studies. One might expect spurious signals resulting from diffractions to smear out and reduce in amplitude in actual CCP stacks constructed using waveforms from many different ray parameters in the same range. However, additional waveforms from ray parameters that fill in between the ones we have tested would not in fact introduce any additional smearing, since their waveform effects will be intermediate to those we have already accounted for. Indeed, if one considers that the typical distribution of ray parameters recorded at a seismic station is far more peaked around one or two ray parameter ranges than our distribution (which represents uniform likelihood of encountering the range of possible ray parameters), it would not be unreasonable to expect that typical spurious signal amplitudes be even greater than those represented in our stacks. Of course, 3-D effects might work to attenuate the diffraction signals. The 2-D geometry of our wavefield simulations limits our ability to quantitatively predict the exact artefacts expected to arise in settings where 3-D variations in lithospheric structure are pronounced. Our results, however, should motivate future, systematic, numerical investigations in 3-D geometries, which present computational challenges that are beyond the scope of our work.

4.4 Effects of noise

We have not explicitly accounted for effects of noise on Sp analysis. This is not because the effects of noise are minor; indeed, relatively low signal-to-noise ratios are a key limitation on Sp imaging of the

lithosphere. Previous investigations have found that the common assumption of white noise can be woefully inadequate for modelling the effects of noise on Sp RFs (e.g. Kolb & Lekić 2014). Furthermore, they found that the coloured noise present near the dominant period typical for Sp analyses (8 s, and achieved by filtering our synthetic waveforms with a 0.03–0.125 Hz passband) is effective at introducing artefacts into Sp RFs, which can be suppressed by the explicit treatment of noise in the Sp deconvolution. Furthermore, the dominant sources of seismic noise in this period band can vary strongly with location and time (see, e.g. Stutzmann *et al.* 2012; Koper & Burlacu 2015). This variability implies that the effects of noise on Sp waveforms, RFs, and CCP stacks are likely to vary across studies and not be straightforwardly generalizable.

5 CONCLUSIONS

Using synthetic waveforms computed through a suite of idealized models of lithospheric structure, we have systematically studied the ability of Sp RFs and CCP stacks to image lithospheric structure in the presence of lateral variations in lithospheric thickness. These tests confirm that interpreting certain aspects of Sp CCP stacks can be intuitive; for example, resolving power decreases at longer periods, shallow-dipping ($<7^\circ$) interfaces are easier to image than steeply dipping ones, and side-lobes can be more prominent when performing frequency domain deconvolution with band-limited data. The consequences of time-domain windowing of the Sp waveforms prior to deconvolution (especially ETMTM and IFD deconvolution), though experientially familiar, have not been well documented in the literature. Finally, we confirm that a station spacing of 80 km, similar to that used by the Transportable Array within the lower 48 states, is sufficient to yield meaningful Sp CCP stacks even in the presence of laterally varying variations in lithospheric thickness, as noted in previous studies (e.g. Lekić & Fischer 2014, suppl. fig. 6).

However, we find that other features of the Sp CCP stacks are not so straightforward to interpret, since they can misrepresent true structural variations and cause spurious intralithospheric layering. When considering structures with asymmetric variations in lithospheric thickness, we show that illumination direction—and, to a lesser extent, the ray parameter of the parent wavefield—affects the appearance of interfaces, particularly when the slope of the LAB topography is larger than approximately 7° . Though gently dipping LAB topography can be reliably retrieved regardless of illumination direction, steeply sloped topography appears artificially gently dipping when illumination is from the side with thicker lithosphere. Furthermore, LAB topography can produce duplexed Sp phases that are mapped into multiple LAB-like interfaces. The horizontal extent of such duplexed phases increases with topography slope and with ray parameter. Though this duplexing is present with both illumination directions, it is more pronounced when illumination is from the side with thicker lithosphere. On the other hand, illumination from the side with thinner lithosphere can produce a pronounced reversed-polarity phase that can mimic a mid-lithosphere velocity (impedance) increase, and the relatively weak conversion coefficient across the dipping stretch of the LAB can result in the LAB appearing discontinuous in CCP stacks.

We show that the duplexed and reverse-polarity Sp phases result from *S*-to-*P* waves diffractions produced at the corners in LAB topography. We illustrate how these phases can lead to an unexpected asymmetry in Sp CCP imaging of regions of thickened versus thinned lithosphere: localized lithospheric thinning is more difficult

to unequivocally pin down in *Sp* CCP stacks because the corner diffractions make the deeper LAB appear continuous across the thinned region, while localized thickening is rendered more prominent, since the corner diffractions extend its apparent lateral extent. Along-section distribution of spurious intra-lithospheric velocity-increase-with-depth interfaces will depend on illumination geometry and the lateral variations in structure. On a positive note, targeted identification and analysis of these diffracted phases, which will tend to be strongest in the vicinity of thinner lithosphere, may represent a secondary observable to confirm or rule out inferences of lithospheric thinning drawn from *Sp* CCP stacks. Numerical waveform simulations show that corner diffractions are muted in amplitude when lateral variations in velocity occur across horizontal distances greater than 150 km (Mancinelli & Fischer 2016). Therefore, by choosing to study the *Sp* wavefield effects of models with sharp corners, we have estimated the maximum effect of possible corner diffractions; in the mantle such structures may be smoother and the effects smaller. Indeed, strong spatial velocity gradients needed to produce the corner diffractions are unlikely to be ubiquitous in the mantle lithosphere. However, in regions where strong conversions across the seismic LAB indicate the presence of accumulated melt (e.g. Hopper *et al.* 2014), seismic velocity variations accompanying variations in melt content may indeed be sufficiently sharp to produce diffracted waves.

In short, caution should be exercised when interpreting *Sp* waveforms, RFs, and CCP stacks in the presence of lateral variations in lithospheric structure, and, ideally, signals and images formed from different illumination directions and ray parameter bins should be compared to distinguish spurious from actual variations in lithospheric structure.

ACKNOWLEDGEMENTS

We thank the SPEC-FEM2D team and the Computational Infrastructure for Geodynamics for providing the code with useful examples. We also thank S. Burdick for helpful comments on this manuscript. VL acknowledges support from the National Science Foundation (CAREER grant EAR1352214) and from the Packard Fellowship for Science and Technology.

REFERENCES

- Abt, D., Fischer, K., French, S., Ford, H., Yuan, H. & Romanowicz, B., 2010. North American lithospheric discontinuity structure imaged by *Ps* and *Sp* receiver functions, *J. geophys. Res.*, **115**, B09301, doi:10.1029/2009JB006914.
- Alsina, D. & Snieder, R., 1995. Small-scale sublithospheric continental mantle deformation: constraints from SKS splitting observations, *Geophys. J. Int.*, **123**, 431–448.
- Ammon, C.J., 1991. The isolation of receiver effects from teleseismic *p* waveforms, *Bull. seism. Soc. Am.*, **81**(6), 2504–2510.
- Angus, D.A., Wilcon, D.C., Sandvol, E. & Ni, J.F., 2006. Lithospheric structure of the Arabian and Eurasian collision zone in eastern Turkey from *S*-wave receiver functions, *Geophys. J. Int.*, **166**, 1335–1346.
- Bostock, M., 1998. Mantle stratigraphy and evolution of the Slave province, *J. geophys. Res.*, **103**(B9), 21 183–21 200.
- Bostock, M., Rondenay, S. & Shragge, J., 2001. Multiparameter two-dimensional inversion of scattered teleseismic body waves: 1. Theory for oblique incidence, *J. geophys. Res.*, **106**(B12), 30 771–30 782.
- Burdick, L.J. & Langston, C.A., 1977. Modeling crustal structure through the use of converted phases in teleseismic body-wave forms, *Bull. seism. Soc. Am.*, **67**(3), 677–691.
- Burdick, S., de Hoop, M.V., Wang, S. & van der Hilst, R., 2013. Reverse-time migration-based reflection tomography using teleseismic free surface multiples, *Geophys. J. Int.*, **196**, 996–1017.
- Chen, L., Zheng, T.Y. & Xu, W.W., 2006. A thinned lithospheric image of the Tanlu Fault Zone, eastern China: constructed from wave equation based receiver function migration, *J. geophys. Res.*, **111**, B09312, doi:10.1029/2005JB003974.
- Chen, L., Cheng, C. & Wei, Z., 2009. Seismic evidence for significant lateral variations in lithospheric thickness beneath the central and western north China craton, *Earth planet. Sci. Lett.*, **286**(1), 171–183.
- Deng, K. & Zhou, Y., 2015. Wave diffraction and resolution of mantle transition zone discontinuities in receiver function imaging, *Geophys. J. Int.*, **201**, 2008–2025.
- Dettmer, J., Dosso, S.E., Bodin, T., Stipčević, J. & Cummins, P.R., 2015. Direct-seismogram inversion for receiver-side structure with uncertain source–time functions, *Geophys. J. Int.*, **203**(2), 1373–1387.
- Dueker, K.G. & Sheehan, A.F., 1997. Mantle discontinuity structure from midpoint stacks of converted *P* to *S* waves across the Yellowstone hotspot track, *J. geophys. Res.*, **102**, 8313–8327.
- Farra, V. & Vinnik, L., 2000. Upper mantle stratification by *P* and *S* receiver functions, *Geophys. J. Int.*, **141**(3), 699–712.
- Ford, H., Fischer, K., Abt, D., Rychert, C. & Elkins-Tanton, L., 2010. The lithosphere–asthenosphere boundary and cratonic lithospheric layering beneath Australia from *Sp* wave imaging, *Earth planet. Sci. Lett.*, **300**(3), 299–310.
- Gao, W., Grand, S.P., Baldrige, W.S., Wilson, D., West, M., Ni, J.F. & Aster, R., 2004. Upper mantle convection beneath the central Rio Grande rift imaged by *P* and *S* wave tomography, *J. geophys. Res.*, **109**, B03305 doi:10.1029/2003JB002743.
- Hansen, S.M., Dueker, K. & Schmandt, B., 2015. Thermal classification of lithospheric discontinuities beneath USArray, *Earth planet. Sci. Lett.*, **431**, 36–47.
- Helffrich, G., 2006. Extended-time multitaper frequency domain cross-correlation receiver-function estimation, *Bull. seism. Soc. Am.*, **96**(1), 344–347.
- Hopper, E. & Fischer, K.M., 2015. The meaning of midlithospheric discontinuities: a case study in the northern US craton, *Geochem. Geophys. Geosyst.*, **16**(12), 4057–4083.
- Hopper, E., Ford, H.A., Fischer, K.M., Lekić, V. & Fouch, M.J., 2014. The lithosphere–asthenosphere boundary and the tectonic and magmatic history of the northwestern United States, *Earth planet. Sci. Lett.*, **402**, 69–81.
- Kennett, B. & Engdahl, E., 1991. Traveltimes for global earthquake locations and phase identifications, *Geophys. J. Int.*, **105**, 429–465.
- Kind, R., Yuan, X. & Kumar, P., 2012. Seismic receiver functions and the lithosphere–asthenosphere boundary, *Tectonophysics*, **536–537**, 25–43.
- Kolb, J. & Lekić, V., 2014. Receiver function deconvolution using trans-dimensional hierarchical Bayesian inference, *Geophys. J. Int.*, **197**(3), 1719–1735.
- Komatitsch, D. & Tromp, J., 2002. Spectral-element simulations of global seismic wave propagation—II. Three-dimensional models, oceans, rotation and self-gravitation, *Geophys. J. Int.*, **150**, 303–318.
- Komatitsch, D. & Vilotte, J., 1998. The spectral element method: an efficient tool to simulate the seismic response of 2D and 3D geological structures, *Bull. seism. Soc. Am.*, **88**(2), 368–392.
- Koper, K.D. & Burlacu, R., 2015. The fine structure of double-frequency microseisms recorded by seismometers in North America, *J. geophys. Res.*, **120**(3), 1677–1691.
- Kvasnička, M. & Vlastislav, Č., 1996. Analytical expressions for Fresnel volumes and interface Fresnel zones of seismic body waves. Part 2: Transmitted and converted waves. Head waves, *Stud. Geophys. Geod.*, **40**(4), 381–397.
- Lekić, V. & Fischer, K.M., 2014. Contrasting lithospheric signatures across the western United States revealed by *Sp* receiver functions, *Earth planet. Sci. Lett.*, **402**, 90–98.
- Lekić, V., French, S. & Fischer, K., 2011. Lithospheric thinning beneath rifted regions of southern California, *Science*, **334**(6057), 783–787.

- Levander, A. & Miller, M., 2012. Evolutionary aspects of lithosphere discontinuity structure in the western us, *Geochem. Geophys. Geosyst.*, **13**, Q0AK07, doi:10.1029/2012GC004056.
- Levander, A., Niu, F. & Symes, W., 2005. Imaging teleseismic p to s scattered waves using the Kirchhoff integral, *Geophys. Monogr. Ser.*, **157**, 149–169.
- Li, X., Yuan, X. & Kind, R., 2007. The lithosphere–asthenosphere boundary beneath the western united states, *Geophys. J. Int.*, **170**(2), 700–710.
- Ligorria, J.P. & Ammon, C.J., 1999. Iterative deconvolution and receiver-function estimation, *Bull. seism. Soc. Am.*, **89**(5), 1395–1400.
- Mancinelli, N. & Fischer, K.M., 2016. Observing and modeling frequency-dependence in Sp receiver functions: implications for the continental lithosphere, *AGU Fall Meeting*, D141D-03.
- Miller, M.S. & Eaton, D.W., 2010. Formation of cratonic mantle keels by arc accretion: evidence from S receiver functions, *Geophys. Res. Lett.*, **37**(18), doi:10.1029/2010GL044366.
- Park, J. & Levin, V., 2000. Receiver functions from multiple-taper spectral correlation estimates, *Bull. seism. Soc. Am.*, **90**(6), 1507–1520.
- Poppeliers, C. & Pavlis, G.L., 2003. Three-dimensional, prestack, plane wave migration of teleseismic P-to-S converted phases: 1. Theory, *J. geophys. Res.*, **108**(B2), 2112, doi:10.1029/2001JB000216.
- Reeves, Z., Lekić, V., Schmerr, N., Kohler, M. & Weeraratne, D., 2015. Lithospheric structure across the California continental borderland from receiver functions, *Geochem. Geophys. Geosyst.*, **16**(1), 246–266.
- Revenaugh, J., 1995. The contribution of topographic scattering to teleseismic coda in southern California, *Geophys. Res. Lett.*, **22**(5), 543–546.
- Rondenay, S., 2009. Upper mantle imaging with array recordings of converted and scattered teleseismic waves, *Surv. Geophys.*, **30**(4–5), 377–405.
- Rondenay, S., Bostock, M.G. & Fischer, K.M., 2005. Multichannel inversion of scattered teleseismic body waves: practical considerations and applicability, in *Seismic Earth: Array Analysis of Broadband Seismograms*, Geophysical Monograph Series 158, pp. 187–203, doi:10.1029/157GM12.
- Rychert, C. & Shearer, P., 2009. A global view of the lithosphere–asthenosphere boundary, *Science*, **324**(5926), 495–498.
- Rychert, C.A., Shearer, P.M. & Fischer, K.M., 2010. Scattered wave imaging of the lithosphere–asthenosphere boundary, *Lithos*, **120**(1), 173–185.
- Shearer, P.M., 1991. Constraints on upper mantle discontinuities from observations of long-period reflected and converted phases, *J. geophys. Res.*, **96**(B11), 18 147–18 182.
- Sheehan, A.F., Shearer, P.M., Gilbert, H.J. & Dueker, K.G., 2000. Seismic migration processing of P–SV converted phases for mantle discontinuity structure beneath the snake river plain, western united states, *J. geophys. Res.*, **105**(B8), 19 055–19 065.
- Shibutani, T., Ueno, T. & Hirahara, K., 2008. Improvement in the extended-time multitaper receiver function estimation technique, *Bull. seism. Soc. Am.*, **98**(2), 812–816.
- Spetzler, J. & Snieder, R., 2001. The effect of small-scale heterogeneity on the arrival time of waves, *Geophys. J. Int.*, **145**, 786–796.
- Stutzmann, E., Arduin, F., Schimmel, M., Mangeny, A. & Patau, G., 2012. Modelling long-term seismic noise in various environments, *Geophys. J. Int.*, **191**(2), 707–722.
- Vinnik, L., 1977. Detection of waves converted from P to SV in the mantle, *Phys. Earth planet. Inter.*, **15**, 39–45.
- Vinnik, L., Kozlovskaya, E., Oreshin, S., Kosarev, G., Piiponen, K. & Silvenoinen, H., 2016. The lithosphere, LAB, LVZ and Lehmann discontinuity under central Fennoscandia from receiver functions, *Tectonophysics*, **667**, 189–198.
- Wilson, D. & Aster, R., 2005. Seismic imaging of the crust and upper mantle using regularized joint receiver functions, frequency–wave number filtering, and multimode Kirchhoff migration, *J. geophys. Res.*, **110**, B05305, doi:10.1029/2004JB003430.
- Wilson, D., Angus, D., Ni, J. & Grand, S., 2006. Constraints on the interpretation of S-to-P receiver functions, *Geophys. J. Int.*, **165**(3), 969–980.
- Wittlinger, G. & Farra, V., 2007. Converted waves reveal a thick and layered tectosphere beneath the Kalahari super-craton, *Earth planet. Sci. Lett.*, **254**, 404–415.
- Wittlinger, G., Farra, V. & Vergne, J., 2004. Lithospheric and upper mantle stratifications beneath Tibet: new insights from Sp conversions, *Geophys. Res. Lett.*, **31**, L19615, doi:10.1029/2004GL020955.
- Wölbner, I., Rümpker, G., Link, G.K. & Sodoudi, F., 2012. Melt infiltration of the lower lithosphere beneath the Tanzania craton and the Albertine rift inferred from S receiver functions, *Geochem. Geophys. Geosyst.*, **13**, Q0AK08, doi:10.1029/2012GC004167.